Nd^{3+}-Sensitized Upconversion Nanophosphors: Efficient *In Vivo* Bioimaging Probes with Minimized Heating Effect

Ye-Fu Wang, Gao-Yuan Liu, Ling-Dong Sun,* Jia-Wen Xiao, Jia-Cai Zhou, and Chun-Hua Yan*

Beijing National Laboratory for Molecular Sciences, State Key Laboratory of Rare Earth Materials Chemistry and Applications & PKU-HKU Joint Laboratory in Rare Earth Materials and Bioinorganic Chemistry, College of Chemistry and Molecular Engineering, Peking University, Beijing 100871, China

ABSTRACT Upconversion (UC) process in lanthanide-doped nanomaterials has attracted great research interest for its extensive biological applications *in vitro* and *in vivo*, benefiting from the high tissue penetration depth of near-infrared excitation light and low autofluorescence background. However, the 980 nm laser, typically used to trigger the Yb^{3+}-sensitized UC process, is strongly absorbed by water in biological structures and could cause severe overheating effect. In this article, we report the extension of the UC excitation spectrum to shorter wavelengths, where water has lower absorption. This is realized by further introducing Nd^{3+} as the sensitizer and by building a core/shell structure to ensure successive $Nd^{3+}\rightarrow Yb^{3+}\rightarrow$activator energy transfer. The efficacy of this Nd^{3+}-sensitized UC process is demonstrated in *in vivo* imaging, and the results confirmed that the laser-induced local overheating effect is greatly minimized.

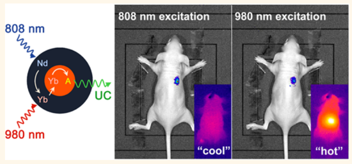

KEYWORDS: upconversion · excitation band extension · heating effect · *in vivo* imaging

During the past few years, lanthanide nanoparticles (NPs) with upconversion (UC) emission have attracted extensive research interests.[1−4] Typically, these NPs are simultaneously doped with sensitizers (usually Yb^{3+}) and activators (Er^{3+}, Tm^{3+}, or Ho^{3+} in most cases).[5−8] The sensitizers absorb near-infrared (NIR) photons and then transfer the energy to the activators.[9,10] Successive absorption of NIR photons and/or energy transfer (ET) will promote the activators to higher excited states and eventually lead to radiation of higher-energy photons located in the ultraviolet, visible, or NIR region.[11−13] The relatively high penetration depth of NIR light in biological structures, minimized autofluorescence background, and low biotoxicity qualify UCNPs as promising probes for a variety of biological applications,[14,15] including sensing,[16,17] imaging,[18,19] and therapy.[20,21]

However, the narrow band absorption nature of the Yb^{3+}-sensitized UC process imposes challenges to the *in vivo* applications.[22] Yb^{3+} has only one excited state ($^2F_{5/2}$), which results in the absorption band located at *ca.* 980 nm ($^2F_{7/2}\rightarrow{}^2F_{5/2}$). This band coincides with the strong absorption of water (Figure 1),[23] the most concentrated and significant NIR absorber in biological tissues. Continuous laser irradiation at 980 nm to trigger the UC process would lead to a risk of local temperature rise, and substantial overheating may even induce cell and tissue damage.[24] This non-negligible risk puts a major obstacle for the *in vivo* applications of UCNPs, especially when long-duration or high-power-density laser exposure is needed. Although excitation at 900−1000 nm for Yb^{3+} and even longer excitation wavelength for Er^{3+} at 1522 nm have been proposed with the sacrifice of upconversion efficiency,[24,25] it is still far from applications with flexibility. Dye-sensitized upconversion emission, utilizing the Förster energy transfer,[22] inspired us to develop a strategy to shift the excitation to a shorter wavelength without compromising the excitation efficiency.

Here, to address the issue of NIR laser-induced tissue damage, we further introduce Nd^{3+} ions as new NIR absorbers and sensitizers in the conventional Yb^{3+}-doped UCNPs. It has been reported that the $Nd^{3+}\rightarrow Yb^{3+}$ ET has high efficiencies in different types of host materials (up to 70%, corresponding to the proportion of Nd^{3+}

* Address correspondence to
sun@pku.edu.cn;
yan@pku.edu.cn.

Received for review May 23, 2013
and accepted July 19, 2013.

10.1021/nn402601d

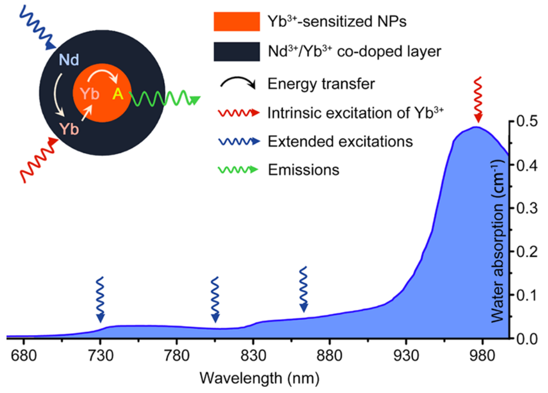

Figure 1. Absorption of water in the NIR and the integration scheme of $Nd^{3+}\rightarrow Yb^{3+}$ ET process by introducing Nd^{3+}/Yb^{3+} co-doped shell. The resulting $Nd^{3+}\rightarrow Yb^{3+}\rightarrow$activator ET could extend the effective excitation bands for conventional Yb^{3+}-sensitized UCNPs. Featuring lower water absorptions, these alternative excitation bands are expected to minimize the tissue overheating effect caused by NIR laser exposure (blue line represents absorption spectrum of water).

undergoing ET among all excited Nd^{3+} ions).[26−28] This effective ET process is expected to extend the excitation of the conventional Yb^{3+}-doped UCNPs, from the band characteristic of Yb^{3+} to those of Nd^{3+}.

Notably, Nd^{3+} has multiple NIR excitation bands at wavelengths shorter than 980 nm, such as 730, 808, and 865 nm, corresponding to transitions from $^4I_{9/2}$ to $^4F_{7/2}$, $^4F_{5/2}$, and $^4F_{3/2}$, respectively. At all of these wavelengths, water absorption is lower (blue arrows in Figure 1), and the typical absorption coefficient is 0.02 cm^{-1} at 808 nm, in contrast to 0.48 cm^{-1} at 980 nm (red arrow in Figure 1).[26] Consequently, the laser-induced heating effect, especially for biological tissues, is expected to be greatly minimized.[29] Meanwhile, Nd^{3+} has a large absorption cross section in the NIR region (1.2×10^{-19} cm^2 at 808 nm)[30] compared to that of Yb^{3+} (1.2×10^{-20} cm^2 at 980 nm),[31] which also benefits the efficiency of the Nd^{3+}-sensitized UC process.

However, despite the large absorption cross section of Nd^{3+} and the high $Nd^{3+}\rightarrow Yb^{3+}$ ET efficiency, the introduction of Nd^{3+} as sensitizer may directly quench the UC emission, owing to the deleterious ET between activators and Nd^{3+}.[3] To address this concern, spatially separating the activator and Nd^{3+} is necessary. Core/shell structure, which could separate the activator and Nd^{3+} in the core and shell, respectively, is a promising way to avoid such an ET process.[32] As shown in the scheme in Figure 1, the core is doped with Yb^{3+} and activators, where the $Yb^{3+}\rightarrow$activators UC process is supposed to occur, and the shell is doped with Nd^{3+} and Yb^{3+} simultaneously, where the excitation of Nd^{3+} and subsequent $Nd^{3+}\rightarrow Yb^{3+}$ ET could take place. By adopting this core/shell structure, successive $Nd^{3+}\rightarrow Yb^{3+}\rightarrow$activator ET would be dominant, and UC efficiency comparable with that of the Yb^{3+}-sensitized UC process could be expected.

RESULTS AND DISCUSSION

Characterization of Core/Shell NPs. To verify the efficacy of this designed core/shell structure, we prepared the corresponding nanostructures using a general pyrolysis method.[33] First, we obtained $NaGdF_4$:Yb,Er NPs as the core component (13.6 ± 1.2 nm, Figure S1 in Supporting Information (SI)). Then Nd^{3+} is introduced by overgrowing a $NaGdF_4$:Nd,Yb shell layer on the core NPs. As shown in Figure 2a, the as-obtained $NaGdF_4$:Yb,Er@$NaGdF_4$:Nd,Yb NPs (denoted as Er@Nd NPs hereafter) are of uniform size (22.5 ± 1.1 nm), implying a shell thickness of *ca.* 4 nm. The energy-dispersive X-ray spectroscopy (EDS) line-scan profile of a single NP[34,35] (inset of Figure 2a) also revealed a higher concentration of Nd^{3+} at both ends of the line, indicating Nd^{3+} distribution in the shell layer.

UC Process Analysis. UC properties of the Er@Nd NPs are examined with the excitation of 808 and 980 nm diode lasers with the same power (1.5 W) and power density (20 W/cm^2). As shown in Figure 2b, in both cases, the NPs gave intense green (540 nm, Er^{3+}: $^2H_{11/2}$, $^4S_{3/2}\rightarrow {}^4I_{15/2}$) and red (650 nm, Er^{3+}: $^4F_{9/2}\rightarrow {}^4I_{15/2}$) emissions, with the spectral profile, intensity, and red-to-green emission ratio all quite similar. We also measured the power-dependent emission intensities of the green one ($^2H_{11/2}$, $^4S_{3/2}\rightarrow {}^4I_{15/2}$) under excitation at either 808 or 980 nm. As shown in Figure S2 in SI, a slope close to 2 in the log−log scale was obtained, revealing a two-photon UC process. This result indicates that the integration of the $Nd^{3+}\rightarrow Yb^{3+}$ ET process (under 808 nm excitation) does not influence the subsequent $Yb^{3+}\rightarrow Er^{3+}$ UC process, neither in its photodynamic mechanism nor in the emission intensities.

The extension of excitation bands of Yb^{3+}-sensitized UCNPs is further demonstrated in Figure 2c, which shows the excitation spectrum of Er@Nd NPs. Besides the intrinsic excitation of Yb^{3+} at 980 nm ($^2F_{7/2}\rightarrow {}^2F_{5/2}$), three new excitation bands were found in the NIR region, which locate at 730, 808, and 865 nm, corresponding to the transitions of Nd^{3+} from $^4I_{9/2}$ to $^4F_{7/2}$, $^4F_{5/2}$, and $^4F_{3/2}$, respectively. This result is consistent with the absorption spectra of Er@Nd NPs (Figure S3 in SI), which showed an absorption cross section of Nd^{3+} in the NIR region larger than that of Yb^{3+}. It is reasonable to infer that the high absorption cross section of Nd^{3+}, together with the efficient $Nd^{3+}\rightarrow Yb^{3+}$ ET, results in the high excitation efficiency for Nd^{3+}-sensitized UC emission of Er^{3+}.

The proposed ET pathway for Nd^{3+}-sensitized UC emission is shown in Figure 2d. The 808 nm laser excites Nd^{3+} to its $^4F_{5/2}$ state, followed with nonradiative relaxation to the $^4F_{3/2}$ state. The energy could transfer to nearby Yb^{3+} and populate its $^2F_{5/2}$ state and further transfer to nearby Yb^{3+} ions crossing the shell. This ET route would initiate a typical UC process in

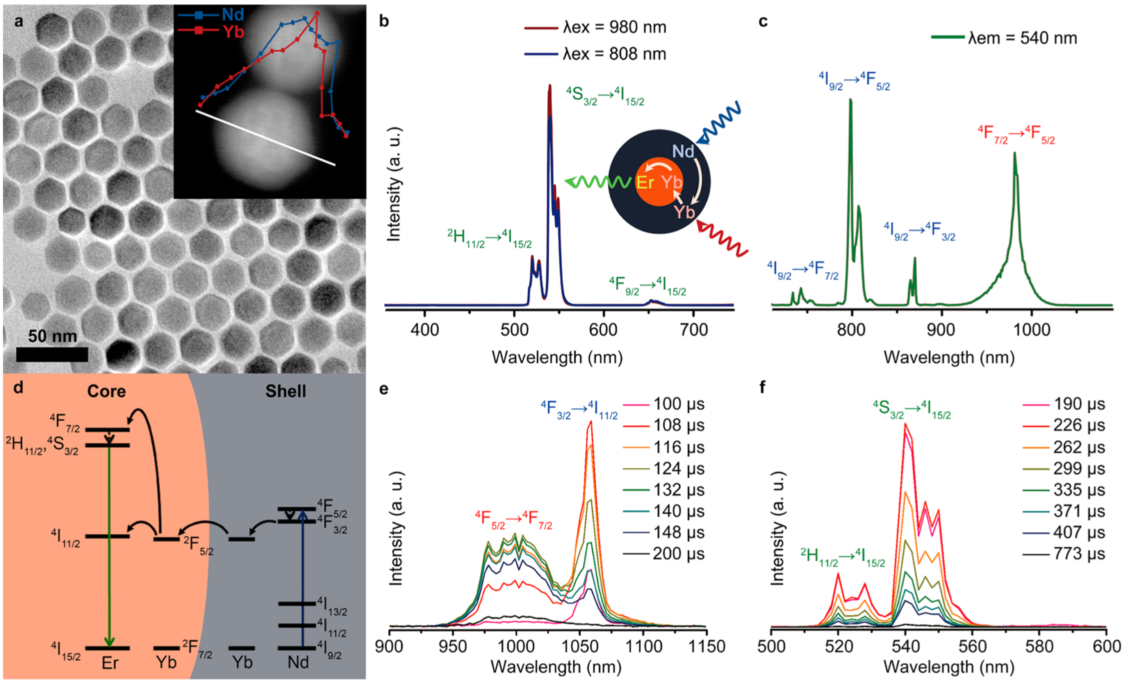

Figure 2. ET in Er@Nd NPs. (a) TEM image of Er@Nd NPs and (inset) EDS line-scan profile of a single particle. (b) UC emission spectra of Er@Nd NPs under 980 and 808 nm excitation. (c) Excitation spectrum of Er@Nd NPs (λ_{em} = 540 nm). (d) ET pathway from Nd^{3+}- to Yb^{3+}-activated Er^{3+} UC emission in core/shell structured NPs under 808 nm excitation. (e,f) Time-resolved emission spectra of Er@Nd NPs under 808 nm excitation. Transitions from Yb^{3+}, Nd^{3+}, and Er^{3+} are denoted in red, blue, and green labels, respectively.

the core, with Er^{3+} ions excited to high-energy states like $^2H_{11/2}$, $^4S_{3/2}$, and $^4F_{9/2}$. This mechanism is further verified with studies on time-resolved emission spectra.[36] As shown in Figure 2e,f, under 808 nm excitation, a short-lived intrinsic emission of Nd^{3+} at 1064 nm ($^4F_{3/2}\rightarrow{}^4I_{13/2}$) was first observed with a delay of 100 μs. Accompanying its maximum, emission from Yb^{3+} at 980 nm ($^2F_{5/2}\rightarrow{}^2F_{7/2}$) could be clearly observed. Later, emission from Yb^{3+} reached its maximum at 124 μs, along with a decay of Nd^{3+} emission. Eventually after a 200 μs delay, the NIR emission was similar to the steady-state emission spectrum profile (Figure S4 in SI). Meanwhile, the rise of Er^{3+} emission at 520 and 540 nm ($^2H_{11/2}$, $^4S_{3/2}\rightarrow{}^4I_{15/2}$) was detected. This observation confirmed that Yb^{3+} is involved in the Nd^{3+}-sensitized UC process, and the successive rise and decay of typical transitions of these three dopants revealed sequential $Nd^{3+}\rightarrow Yb^{3+}$ and $Yb^{3+}\rightarrow Er^{3+}$ ET pathways under 808 nm excitation.

It is obvious that the introduction of Nd^{3+} is essential to realize the upconversion emission under the excitation of 808 nm. This Nd^{3+}-sensitized UC process is further verified with a series of supplementary experiments. We replaced Nd^{3+} with lanthanide ions X^{3+} (X = Dy, Tm, Pr, Ho) in the core/shell structured NPs. Under irradiation with an 808 nm laser, no detectable UC emission was recorded for all these Er@X NPs (Figure S5 in SI). This is ascribed to the low absorption at 808 nm and/or low $X^{3+}\rightarrow Yb^{3+}$ ET efficiency for X^{3+} ions. These results indicate that Nd^{3+} is an irreplaceable sensitizer for the 808 nm laser-excited UC process. We also found that the emission intensity of Er@Nd NPs increased with the doping concentration of Nd^{3+} up to 10% (Figure S6 in SI), although self-quenching of Nd^{3+} was observed at this concentration.

We also investigated the necessity of Yb^{3+} and the core/shell structure in Nd^{3+}-sensitized UC process. UCNPs without Yb^{3+} doping (namely, $NaGdF_4$:Nd,Er) and UCNPs without core/shell structure (namely, $NaGdF_4$:Nd,Yb,Er) were prepared, and their UC emission properties were examined (Figure S7 in SI). $NaGdF_4$:Nd,Er NPs gave no detectable UC emission under either 808 or 980 nm laser excitation, suggesting the importance of Yb^{3+} for relaying the energy eventually to Er^{3+}. Meanwhile, only weak UC emission was observed for $NaGdF_4$:Nd,Yb,Er NPs, showing that Nd^{3+} might quench the UC emission from Er^{3+} if they are not spatially separated, consistent with previous reports.[3] The co-doping of Yb^{3+} in the shell also benefits the overall upconversion emission (Figure S8 in SI) by connecting the ET from $Nd^{3+}\rightarrow Yb^{3+}$ in the shell to the Yb^{3+} in the core. As a result, to achieve intense UC emission, Yb^{3+} is needed to bridge the successive $Nd^{3+}\rightarrow Yb^{3+}\rightarrow Er^{3+}$ ET, and the core/shell structure is essential to realize the efficient $Nd^{3+}\rightarrow Yb^{3+}$ ET process and subsequent $Yb^{3+}\rightarrow Er^{3+}$ ET process. Note that the Nd^{3+}/Yb^{3+}-doped shell layer here would not prevent quenching of UC emission by the surface quenchers, which makes the NPs susceptible to the environment,

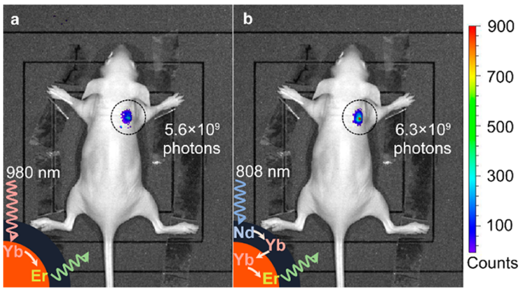

Figure 3. *In vivo* UC imaging of a nude mouse subcutaneously injected with Er@Nd NPs. The images were obtained with 980 nm laser (a) and 808 nm laser (b) irradiation, both with a power density of 200 mW/cm^2. ROIs are denoted in black dot circles.

especially when they are dispersed in water. Further research should be carried out to address this effect.

***In Vivo* Imaging.** Compared to visible and ultraviolet light, NIR light has relatively low tissue absorption (Figure S9 in SI) and thus high penetration depth, which is particularly desirable for detection and imaging. We used a highly scattered agar phantom to test the penetration depth of 808 and 980 nm light, and similar penetration depth limit for both wavelengths was detected (Figure S10 in SI). This observation promises Er@Nd NPs as ideal bioprobes for *in vivo* imaging under 808 nm irradiation. *In vivo* imaging with Er@Nd NPs was studied by injecting NP dispersion into a nude mouse (20 mg/mL, 50 μL). A typical image is shown in Figure 3 with irradiation of 808 and 980 nm laser (power density of *ca.* 200 mW/cm^2). Numbers of photons emitted from the same region of interest (ROI) were found to be comparable (6.3×10^9 for 808 nm excitation and 5.6×10^9 for 980 nm). This implies that 808 nm laser excitation is as efficient for *in vivo* applications of Er@Nd NPs.

Besides excitation of $^4I_{9/2} \rightarrow {}^4F_{5/2}$ at 808 nm, another excitation band at 730 nm (Nd^{3+}: $^4I_{9/2} \rightarrow {}^4F_{7/2}$) was also used to demonstrate the *in vivo* imaging using Er@Nd NPs (Figure S11 in SI). This multiple excitation characteristic could make the Er@Nd NPs more flexible in applications. Furthermore, UC probes with different emissions are feasible by introducing different activators. For example, $NaGdF_4$:Yb,Tm@$NaGdF_4$:Nd,Yb NPs (denoted as Tm@Nd NPs hereafter) could give intense characteristic emission at 475 nm under 808 nm excitation (Figure S12 in SI). Also, Er@Nd NPs and Tm@Nd NPs could give multicolor *in vivo* imaging under 808 nm laser irradiation, as demonstrated in the right back and left back of a nude mouse, respectively (Figure S13 in SI).

Heating Effect Evaluation. It is expected that the extension of excitation bands to shorter wavelengths would minimize the laser-induced heating effect by diminishing the absorption by water. Here, the NPs were transferred into the water phase with earlier reported methods,[37] giving a hydrodynamic diameter of 30.0 ± 2.0 nm (Figure S14 in SI). Under continuous laser irradiation, laser-power-dependent temperature rise profiles were recorded (Figure S15a in SI). A temperature rise of *ca.* 10 °C was observed for samples (5 mg UCNP per mL) under irradiation of a 980 nm laser for 10 min, in contrast to *ca.* 2 °C under 808 nm laser (both at a power density of 35 W/cm^2). These profiles are consistent with those of deionized water (Figure S15b in SI).

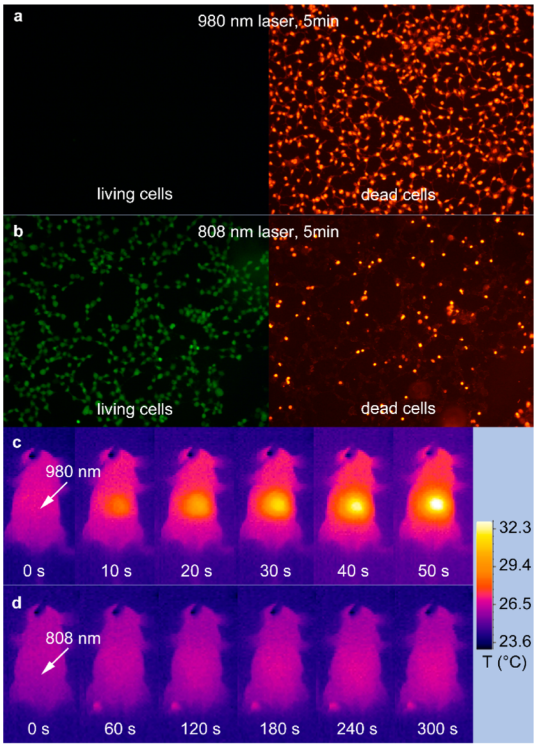

Figure 4. *In vitro* and *in vivo* heating effect induced by laser irradiation. (a,b) HEK 293T cells after 5 min irradiation of 980 nm (a) and 808 nm laser (b). Living cells and dead cells were stained with calcein AM and propidium iodide, respectively. (c,d) Infrared thermal image of a nude mouse during continuous (c) 980 nm laser irradiation for 50 s and (d) 808 nm laser irradiation for 300 s. Irradiation spots are denoted with the white arrows.

The heating effects for 808 and 980 nm lasers were further studied on HEK 293T cells. The cell vitality under laser irradiation (power density of 400 mW/cm^2 for both lasers) for 5 min clearly shows that almost all cells were dead after 980 nm laser irradiation (Figure 4a), while most of the cells survived the 808 nm laser irradiation (Figure 4b).

The *in vivo* heating effect experiments were carried out on a nude mouse. With a power density of 130 mW/cm^2 for the lasers, the temperature change was monitored with an infrared thermal imager. Notably, owing to the scattering of animal tissues, the rise in temperature is much faster than that in water. A notable local heating effect and significant rise in temperature (*ca.* 7 °C, Figure 4c) were observed under irradiation of the 980 nm laser for 50 s, and a burn wound was discernible 1 day after irradiation. In contrast, for the

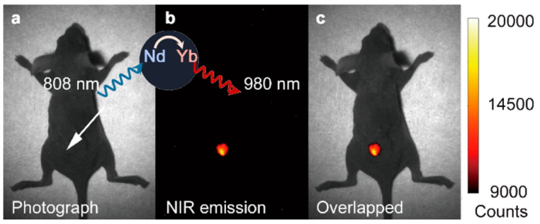

Figure 5. *In vivo* **NIR imaging of a nude mouse injected with Er@Nd NPs dispersed in water. (a) White-light photograph, (b) NIR image obtained with 808 nm excitation, and (c) overlapped image. Injection site is denoted with the white arrow.**

808 nm laser irradiation for as long as 5 min, only a slight rise in temperature for the whole mouse body (*ca.* 1 °C, Figure 4d) was detected. It should also be noted that, for 808 nm irradiation, a larger portion of incident photons is absorbed by hemoglobin, instead of water, compared to the case for 980 nm lasers. Also, the heat dissipation is supposed to be greatly accelerated by the fast blood circulation, and this is further beneficial for minimizing the local overheating with continuous laser exposure.

Down-Shifting Photoluminescence. Besides the UC process, down-shifting photoluminescence (PL) of lanthanide-doped NPs is also of great interest for applications as NIR-to-NIR *in vivo* probes.[38,39] Here, Er@Nd NPs with the excitation of Nd^{3+} and emission from Yb^{3+}, both located in the NIR region, are promising because of the high penetration depth and low autofluorescence background. As shown in Figure S4, the Er@Nd NPs under 808 nm excitation showed intense emission at 980 nm ($^2F_{5/2} \rightarrow {}^2F_{7/2}$) from Yb^{3+}, along with emissions from Nd^{3+} at 1064 nm ($^4F_{3/2} \rightarrow {}^4I_{13/2}$) and 1532 nm ($^4I_{13/2} \rightarrow {}^4I_{15/2}$). NIR image from mouse injected with Er@Nd NPs shows high signal-to-noise ratio under 808 nm laser excitation (Figure 5). The above results indicate that these NPs hold the promise to serve as efficient dual-channel *in vivo* probes using a single excitation source (808 nm laser). The three-dimensional excitation/emission spectrum of Er@Nd NPs in the NIR region (Figure S16 in SI) further revealed several extended excitation bands resulting from Nd^{3+}, including 575 nm ($^4I_{9/2} \rightarrow {}^4G_{5/2}$) and 730 nm ($^4I_{9/2} \rightarrow {}^4F_{7/2}$). These excitation bands not only enrich the down-shifting PL studies but also possess potential *in vivo* applications.

CONCLUSION

In summary, we have integrated $Nd^{3+} \rightarrow Yb^{3+}$ ET to conventional Yb^{3+}-sensitized UC processes as a versatile strategy to extend the single NIR excitation bands for Yb^{3+} to shorter wavelengths. These new excitation bands, especially the one located at 808 nm, could achieve high UC excitation efficiency similar to that of 980 nm excitation, but with greatly minimized tissue overheating effect. Also, the $Nd^{3+} \rightarrow Yb^{3+}$ ET process qualifies Yb^{3+} as a feasible activator in down-shifting PL, which promises a new type of NIR-to-NIR probes for *in vivo* imaging. More importantly, this strategy could be applied in other Yb^{3+}-sensitized UCNPs, regardless of the host materials and dopants. We believe that this strategy offers a "cool" solution for the *in vivo* applications of Yb^{3+}-sensitized nanophosphors and would be inspiring in building novel lanthanide-doped materials.

MATERIALS AND METHODS

Materials. Oleic acid (OA; >90%, Sigma-Aldrich), oleylamine (OM; >80%, Acros), 1-octadecene (ODE; >90%, Acros), trifluoroacetic acid (99%, Acros), trifluoroacetic acid sodium salt (99%, Acros), ethanol (AR), and cyclohexane (AR) were used as received without further purification. BALB/c nude mice were bought from Vital River Co. Ltd., Beijing.

Preparation of $Ln(CF_3COO)_3$. In a typical synthesis, a lanthanide oxide was added into a solution containing slightly excessive trifluoroacetic acid with continuous stirring, which was kept refluxing until an optically transparent solution was formed. The resulting solution was filtered to remove the insoluble materials (if any), and the following solution was dried in an oven at 140 °C for 12 h to obtain $Ln(CF_3COO)_3$ powders.

Synthesis of Er@Nd NPs. Hexagonal-phased $NaGdF_4$:Yb,Er NPs were obtained using the method earlier reported by our group.[33] For synthesis of the core/shell structure, the as-prepared β-$NaGdF_4$:Yb,Er NPs (containing 1 mmol rare earth ions), 1.00 mmol CF_3COONa, 0.80 mmol $Gd(CF_3COO)_3$, 0.10 mmol $Nd(CF_3COO)_3$, and 0.10 mmol $Yb(CF_3COO)_3$ were added to the mixture of 20 mmol OA and 20 mmol ODE in a three-necked flask (100 mL) at room temperature. Then, the slurry was heated to 120 °C to remove water and oxygen with vigorous magnetic stirring under vacuum for several minutes in a temperature-controlled electromantle to form an optically transparent solution. The solution was heated to a temperature to 310 °C at a heating rate of 15 °C/min and kept for 30 min under a N_2 atmosphere. On cooling to room temperature, the nanocrystals were precipitated by adding excess absolute ethanol into the reacted solution and then collected by centrifugation.

Instrumentation. Samples for transmission electron microscopy (TEM) analysis were prepared by drying a drop of nanoparticle dispersion in cyclohexane on amorphous carbon-coated copper grids. TEM characterization on particle sizes and shapes was performed with a JEOL JEM-2100 TEM operated at 200 kV. UC emission spectra were measured by using the Hitachi F-4500 fluorescent spectrometer. Near-infrared (NIR) emission spectra and three-dimensional excitation/emission spectra were measured using an infrared fluorescence spectrometer (Nanolog FL3-2iHR, HORIBA JOBIN YVON), with an 830 nm long-pass filter. Lasers for 808 nm/980 nm excitation are high-power multimode pump lasers (Hi-tech Optoelectronic Co. Ltd., with a maximum power 5.0 W for both lasers). Laser power was measured with an optical power meter. Excitation spectrum and time-resolved emission spectra were tested with a customized UV to mid-infrared steady-state and phosphorescence lifetime spectrometer (FSP920-C, Edinburgh) equipped with a tunable midband OPO pulse laser as excitation source (410−2400 nm, 10 Hz, pulse width ≤5 ns, Vibrant 355II, OPOTEK). The hydrodynamic diameter analysis was carried out on a nanoparticle analyzer (SZ-100, HORIBA JOBIN YVON).

***In Vivo* Imaging.** *In vivo* imaging was carried out in a CALIPER Lumina II *in vivo* imaging system (IVIS). BALB/c nude mice were anesthetized by injecting chloral hydrate (5% aqueous solution, 100 μL) and immobilized on the imaging stage of IVIS. The white-light images and fluorescence images were captured individually. The fluorescence images were taken with 0.1 s exposure time and *f*/8 aperture. External 808 nm/980 nm lasers were introduced with a beam expander, with a 45 °C incident angle. The excitation power densities for both lasers were tuned to 200 mW/cm^2. A 680/SP filter, a 720/SP filter (Semrock, Inc.), and a GRB3 filter (Shijiazhuang Zeyuan Optical Material Co., Ltd.) were used as emission filters for *in vivo* imaging under both 808 and 980 nm excitation. For *in vivo* imaging using 730 nm excitation, an extra 720/SP filter was used. For multicolor imaging, an extra DTB435 filter (Newport Glass Works, Ltd.) was used for blue-light channel imaging, and extra 495/LP and 515/LP filters were used for green-light channel imaging. For NIR *in vivo* imaging, an 808 nm laser with power density of 90 mW/cm^2 was used, and an 880/LP filter was employed to filter the excitation light before the InGaAs camera. The corresponding *in vivo* NIR images were taken with 20 ms exposure time. The NIR-to-NIR photoluminescence image was obtained with an InGaAs array detector (Inter-Diff Co., Ltd.).

***In Vivo* Laser Heating Effect.** BALB/c nude mice were anesthetized by injecting chloral hydrate (5% aqueous solution, 100 μL) and immobilized on the imaging stage of IVIS, and the temperature of the stage was set to 25 °C. External 808 nm/980 nm lasers were introduced with a beam expander, with a 45 °C incident angle. The excitation power densities for both lasers were tuned to 130 mW/cm^2. Thermal images were captured with an infrared thermal imager every 10 s.

Conflict of Interest: The authors declare no competing financial interest.

Acknowledgment. We gratefully thank Prof. Xueyuan Chen and Dr. Haomiao Zhu at Fujian Institute of Research on the Structure of Matter, Chinese Academy of Sciences, for their valuable help in excitation spectra and time-resolved emission spectra measurement. We also gratefully thank Prof. Qiangbin Wang and Dr. Chunyan Li at Suzhou Institute of Nanotech and Nanobiotics, Chinese Academy of Sciences, for their valuable help in NIR *in vivo* imaging. This work was supported by NSFC (Nos. 20971005 and 20931160429) and MOST of China (No. 2011AA03A407).

Supporting Information Available: Experimental details and additional figures (Figures S1−S16). This material is available free of charge *via* the Internet at http://pubs.acs.org.

REFERENCES AND NOTES

1. Wang, F.; Liu, X. Recent Advances in the Chemistry of Lanthanide-Doped Upconversion Nanocrystals. *Chem. Soc. Rev.* **2009**, *38*, 976–989.
2. Chatterjee, D. K.; Gnanasammandhan, M. K.; Zhang, Y. Small Upconverting Fluorescent Nanoparticles for Biomedical Applications. *Small* **2010**, *6*, 2781–2795.
3. Wang, F.; Han, Y.; Lim, C. S.; Lu, Y.; Wang, J.; Xu, J.; Chen, H.; Zhang, C.; Hong, M.; Liu, X. Simultaneous Phase and Size Control of Upconversion Nanocrystals through Lanthanide Doping. *Nature* **2010**, *463*, 1061–1065.
4. Mullen, T. J.; Zhang, M.; Feng, W.; El-khoui, R. J.; Sun, L. D.; Yan, C. H.; Patten, T. E.; Liu, G. Y. Fabrication and Characterization of Rare-Earth-Doped Nanostructures on Surfaces. *ACS Nano* **2011**, *5*, 6539–6545.
5. Sivakumar, S.; van Veggel, F. C. J. M.; Raudsepp, M. Bright White Light through Up-Conversion of a Single NIR Source from Sol−Gel Derived Thin Film Made with Ln^{3+} Doped LaF$_3$ Nanoparticles. *J. Am. Chem. Soc.* **2005**, *127*, 12464–12465.
6. Xue, T.; Zhu, Y.; Wei, W.; Wang, S.; Huang, J.; Naccache, R.; Hu, W.; Tok, I.; Han, Y.; Zhang, Q.; *et al.* Lanthanide-Doped Na$_x$ScF$_{3+x}$ Nanocrystals: Crystal Structure Evolution and Multicolor Tuning. *J. Am. Chem. Soc.* **2012**, *134*, 8340–8343.
7. Ye, X.; Collins, J. E.; Kang, Y.; Chen, J.; Chen, D. T. N.; Yodh, A. G.; Murray, C. B. Morphologically Controlled Synthesis of Colloidal Upconversion Nanophosphors and Their Shape-Directed Self-Assembly. *Proc. Natl. Acad. Sci. U.S.A.* **2010**, *107*, 22430–22435.
8. Wang, F.; Sun, L. D.; Gu, J.; Wan, Y. F.; Feng, W.; Yang, Y.; Wang, J.; Yan, C. H. Selective Heteroepitaxial Nanocrystal Growth of Rare Earth Fluorides on Sodium Chloride: Synthesis and Density Functional Calculations. *Angew. Chem., Int. Ed.* **2012**, *51*, 8796–8799.
9. Schäfer, H.; Haase, M. Upconverting Nanoparticles. *Angew. Chem., Int. Ed.* **2011**, *50*, 5808–5829.
10. Chen, G.; Ohulchanskyy, T. Y.; Kumar, R.; Ågren, H.; Prasad, P. N. Ultrasmall Monodisperse NaYF$_4$:Yb^{3+}/Tm^{3+} Nanocrystals with Enhanced Near-Infrared to Near-Infrared Upconversion Photoluminescence. *ACS Nano* **2010**, *4*, 3163–3168.
11. Mai, H. X.; Zhang, Y. W.; Sun, L. D.; Yan, C. H. Highly Efficient Multicolor Up-Conversion Emissions and Their Mechanisms of Monodisperse NaYF$_4$:Yb,Er Core and Core/Shell-Structured Nanocrystals. *J. Phys. Chem. C* **2007**, *111*, 13721–13729.
12. Liu, N.; Yang, P.; He, F.; Zhang, X.; Gai, S.; Li, C.; Lin, J. Tunable Multicolor and Bright White Emission of One-Dimensional NaLuF$_4$:Yb^{3+},Ln^{3+} (Ln = Er, Tm, Ho, Er/Tm, Tm/Ho) Microstructures. *J. Mater. Chem.* **2012**, *22*, 10889–10899.
13. Jayakumar, M. K. G. Remote Activation of Biomolecules in Deep Tissues Using Near-Infrared-to-UV Upconversion Nanotransducers. *Proc. Natl. Acad. Sci. U.S.A.* **2012**, *109*, 8483–8488.
14. Zhou, J.; Liu, Z.; Li, F. Upconversion Nanophosphors for Small-Animal Imaging. *Chem. Soc. Rev.* **2012**, *41*, 1323–1349.
15. Shen, J.; Sun, L. D.; Yan, C. H. Luminescent Rare Earth Nanomaterials for Bioprobe Applications. *Dalton Trans.* **2008**, 5687–5697.
16. Liu, J.; Liu, Y.; Liu, Q.; Li, C.; Sun, L.; Li, F. Iridium(III) Complex-Coated Nanosystem for Ratiometric Upconversion Luminescence Bioimaging of Cyanide Anions. *J. Am. Chem. Soc.* **2011**, *133*, 15276–15279.
17. Zhang, F.; Shi, Q. H.; Zhang, Y.; Shi, Y.; Ding, K.; Zhao, D.; Stucky, G. D. Fluorescence Upconversion Microbarcodes for Multiplexed Biological Detection: Nucleic acid Encoding. *Adv. Mater.* **2011**, *23*, 3775–3779.
18. Zhou, J. C.; Yang, Z. L.; Dong, W.; Tang, R. J.; Sun, L. D.; Yan, C. H. Bioimaging and Toxicity Assessments of Near-Infrared Upconversion Luminescent NaYF$_4$:Yb,Tm Nanocrystals. *Biomaterials* **2011**, *32*, 9059–9067.
19. Liu, Q.; Sun, Y.; Yang, T.; Feng, W.; Li, C.; Li, F. Sub-10 nm Hexagonal Lanthanide-Doped NaLuF$_4$ Upconversion Nanocrystals for Sensitive Bioimaging *in Vivo*. *J. Am. Chem. Soc.* **2011**, *133*, 17122–17125.
20. Idris, N. M.; Gnanasammandhan, M. K.; Zhang, J.; Ho, P. C.; Mahendran, R.; Zhang, Y. *In Vivo* Photodynamic Therapy Using Upconversion Nanoparticles as Remote-Controlled Nanotransducers. *Nat. Med.* **2012**, *18*, 1580–1585.
21. Yan, B.; Boyer, J. C.; Branda, N. R.; Zhao, Y. Near-Infrared Light-Triggered Dissociation of Block Copolymer Micelles Using Upconverting Nanoparticles. *J. Am. Chem. Soc.* **2011**, *133*, 19714–19717.
22. Zou, W.; Visser, C.; Maduro, J. A.; Pshenichnikov, M. S.; Hummelen, J. C. Broadband Dye-Sensitized Upconversion of Near-Infrared Light. *Nat. Photonics* **2012**, *6*, 560–564.
23. Prahl, S. Optical Properties Spectra; http://omlc.ogi.edu/spectra/index.html (accessed Oct. 17, 2012).
24. Zhan, Q.; Qian, J.; Liang, H.; Somesfalean, G.; Wang, D.; He, S.; Zhang, Z.; Andersson-Engels, S. Using 915 nm Laser Excited Tm^{3+}/Er^{3+}/Ho^{3+}-Doped NaYbF$_4$ Upconversion Nanoparticles for *In Vitro* and Deeper *In Vivo* Bioimaging without Overheating Irradiation. *ACS Nano* **2011**, *5*, 3744–3757.
25. Chen, G. Y.; Ohulchanskyy, T. Y.; Kachynski, Y.; Ågren, H.; Prasad, P. N. Intense Visible and Near-Infrared Upconversion Photoluminescence in Colloidal LiYF$_4$:Er^{3+} Nanocrystals under Excitation at 1490 nm. *ACS Nano* **2011**, *5*, 4981–4986.
26. Weber, M. J. Optical Properties of Yb^{3+} and Nd^{3+}-Yb^{3+} Energy Transfer in YAlO$_3$. *Phys. Rev. B* **1971**, *4*, 3153–3159.
27. Petit, V.; Camy, P.; Doualan, J. L.; Moncorgé, R. CW and Tunable Laser Operation of Yb^{3+} in Nd:Yb:CaF$_2$. *Appl. Phys. Lett.* **2006**, *88*, 051111.

28. Liégard, F.; Doualan, J. L.; Moncorgé, R.; Bettinelli, M. $Nd^{3+} \rightarrow Yb^{3+}$ Energy Transfer in a Codoped Metaphosphate Glass as a Model for Yb^{3+} Laser Operation around 980 nm. *Appl. Phys. B: Laser Opt.* **2005**, *80*, 985–991.
29. Xie, X.; Liu, X. Photonics: Upconversion Goes Broadband. *Nat. Mater.* **2011**, *11*, 842–843.
30. Kushida, T.; Marcos, H. M.; Geusic, J. E. Laser Transition Cross Section and Fluorescence Branching Ratio for Nd^{3+} in Yttrium Aluminum Garnet. *Phys. Rev.* **1968**, *167*, 289–291.
31. Strohhöfer, C. Ph.D. Thesis, Universiteit Utrecht, December 2001.
32. Wang, F.; Deng, R.; Wang, J.; Wang, Q.; Han, Y.; Zhu, H.; Chen, X.; Liu, X. Tuning Upconversion through Energy Migration in Core−Shell Nanoparticles. *Nat. Mater.* **2011**, *10*, 968–973.
33. Mai, H. X.; Zhang, Y. W.; Si, R.; Yan, Z. G.; Sun, L. D.; You, L. P.; Yan, C. H. High-Quality Sodium Rare-Earth Fluoride Nanocrystals: Controlled Synthesis and Optical Properties. *J. Am. Chem. Soc.* **2006**, *128*, 6426–6436.
34. Abel, K. A.; Boyer, J. C.; Andrei, C. M.; van Veggel, F. C. J. M. Analysis of the Shell Thickness Distribution on $NaYF_4$/$NaGdF_4$ Core/Shell Nanocrystals by EELS and EDS. *J. Phys. Chem. Lett.* **2011**, *2*, 185–189.
35. Wang, Y. F.; Sun, L. D.; Xiao, J. W.; Feng, W.; Zhou, J. C.; Shen, J.; Yan, C. H. Rare-Earth Nanoparticles with Enhanced Upconversion Emission and Suppressed Rare-Earth-Ion Leakage. *Chem.—Eur. J.* **2012**, *18*, 5558–5564.
36. Tu, D.; Liu, L.; Ju, Q.; Liu, Y.; Zhu, H.; Li, R.; Chen, X. Time-Resolved FRET Biosensor Based on Amine-Functionalized Lanthanide-Doped $NaYF_4$ Nanocrystals. *Angew. Chem., Int. Ed.* **2011**, *50*, 6306–6310.
37. Dong, A.; Ye, X.; Chen, J.; Kang, Y.; Gordon, T.; Kikkawa, J. M.; Murray, C. B. A Generalized Ligand-Exchange Strategy Enabling Sequential Surface Functionalization of Colloidal Nanocrystals. *J. Am. Chem. Soc.* **2011**, *133*, 998–1006.
38. Chen, G.; Ohulchanskyy, T. Y.; Liu, S.; Law, W. C.; Wu, F.; Swihart, M. T.; Ågren, H.; Prasad, P. N. Core/Shell $NaGdF_4$:Nd^{3+}/$NaGdF_4$ Nanocrystals with Efficient Near-Infrared to Near-Infrared Downconversion Photoluminescence for Bioimaging Applications. *ACS Nano* **2012**, *6*, 2969–2977.
39. Rocha, U.; da Silva, C. J.; Silva, W. F.; Guedes, I.; Benayas, A.; Maestro, L. M.; Elias, M. A.; Bovero, E.; van Veggel, F. C. J. M.; Solé, J. A. G.; *et al.* Subtissue Thermal Sensing Based on Neodymium-Doped LaF_3 Nanoparticles. *ACS Nano* **2013**, *7*, 1188–1199.